Fig.5
SEM images of morphological change of neutrophils
(Bar = 10 μm)
a: Neutrophil with HBSS
b: Activated by TiO_2 particles
c: Activated by Carbon nanotubes
d: Extension of pseudopod and phagocytized particles
e: Atrophied neutrophil
f: Destroyed membrane

Discussions

The study clearly showed the cytotoxicity due to the particle size effect in Ti, TiO_2 and CNT. Micro-nano particles may cause cytotoxicity, although the macroscopic size is quite biocompatible. The increased superoxide content in vivo may affect the cell circumference. The chemical mediators, TNF- alpha and IL-1beta, may induce the inflammatory cascade to affect tissue and organ. The effect is further pronounced by phagocytosis when particles are smaller than cells [7]. The clinical inflammation reaction around the abrasion powders can be well understand by the results obtained in cell functional *in vitro* tests.

Acknowledgements

References

[1] K. Takamura, T. Yamada and Y. Sugioka, et al. : J Biomed Mater Res. Vol 28 (1994), p. 583-9.

[2] Young-kyun Yeo, Seoug-cheul Lim, et al. : J Oral Maxillofac. Surg. Vol 55 (1997), p. 322-326.

[3] A. Rosenberg, K.W. Grätz and H.F. Sailer: J. oral Maxillofac. Surg. Vol 22 (1993), p. 185-188.

[4] Y. Tanimura, F. Watari, et al. : J of Oral and Maxillofacial Surgery. Vol 46(11) (2000), p. 750.

[5] M. Uo, F. Watari, A. Yokoyama, T. Kawasaki, et al. : Biomaterials. Vol 20 (1999), p. 47-55.

[6] F. Takesita, H. Tkata, Y. Ayukawa and T. Suetsugu. : Biomaterials. Vol 18 (1997), p. 21-5.

[7] Kazuchika Tamura, Fumio Watari, et al. : Materials Transactions Vol. 43(12)(2002), p.3052-3057

Quantitative Analysis of Biologic Specimens by X-Ray Scanning Analytic Microscopy

Motohiro Uo, Masaya Tanaka, Fumio Watari

Dental Materials and Engineering, Department of Oral Health Science, Graduate School of Dental Medicine, Hokkaido University, North 13 West 7, Kita-ku, Sapporo 060, Japan

Abstract: X-ray scanning analytic microscopy (XSAM) can be used to visualize the elemental distribution in biologic specimens. In this article, the authors prepared standard specimens for XSAM and performed quantitative analysis of various elements dissolved in soft tissues. Two different types of standard specimens were prepared. Methylmethacrylate (MMA) resin-based standard specimens were prepared with organic compounds of elements for low-concentration standards and lithium borate glass-based standard specimens were prepared with oxides of elements for higher concentration standards. Using these standard specimens, the P and Ca concentrations in normal rat tissue and dissolved Ni, Fe, and Ni concentrations around metal-implanted tissues were quantitatively analyzed. The estimated concentrations of dissolved Fe, Cu, and Ni from the implants were 1000, 40, and 20 mM, respectively. From the concentration levels causing inflammation around these implants, the high toxicity for soft tissue of Ni and Cu at low concentrations, for example, 10 mM, was confirmed. The toxicity of Cu was estimated as next to that of Ni. In contrast, Fe had low toxicity despite high concentrations of dissolved Fe of as much as 1000 mM. In this article, it was possible to estimate the nonmetallic elements and low-concentration metallic elements dispersed in soft tissue by XSAM. © 2004 Wiley Periodicals, Inc. J Biomed Mater Res Part B: Appl Biomater 70B: 146–151, 2004

Keywords: X-ray scanning analytic microscopy (XSAM); quantitative analysis; standard specimen; dissolution; implant; elemental mapping

INTRODUCTION

X-ray scanning analytic microscopy (XSAM) enables elemental distribution analysis for Na to U by energy-dispersive spectroscopy of fluorescent X rays in air without pretreatment even if the sample contains water.[1] This feature is desirable for the analysis of biologic specimens.[2-5] The authors reported application of XSAM for soft-tissue analysis.[2-4] The authors also reported the rapid analysis of metallic dental restoratives.[6] XSAM was useful for visualization of the dissolution and distribution of highly toxic and chemically unstable metal implants in soft tissue. It clearly revealed the dissolved region around pure nickel in soft tissue and showed that it was in good agreement with the highly inflammated tissue region. There is, however, a limitation in that the obtained information is qualitative to semiquantitative. To evaluate dissolved metallic elements in soft tissue, it is necessary to establish concentration standards for each element. The preparation of methylmethacrylate (MMA) resin-based

standard specimens for various elements has been reported.[7] In a previous article,[5] the authors prepared Ni standard specimens with nickel acetylacetonate dispersed in MMA resin and evaluated the Ni dissolution content in soft tissue.

In this article, MMA-based and borate glass-based standard specimens of P, S, Ca, Cr, Mn, Fe, Ni, Cu, and Zn were prepared and subjected to quantitative analysis by XSAM of various elements dissolved in soft tissue.

EXPERIMENTAL PROCEDURE

Preparation of Standards with MMA Resin Matrix

The resin standards for P, S, Ca, Cr, Mn, Fe, Ni, Cu, and Zn were prepared using the organometallic compounds listed in Table I. Each chemical was dissolved in MMA to obtain appropriate concentrations and polymerized at 60°C. For the resin standard, Ca was dissolved as $CaCl_2$ in hydroxyethylmethacrylate (HEMA) and mixed with MMA. Each element was concentrated by the contraction in the polymerization process of MMA. The contraction of MMA was reported to be 21.2%. Therefore, the concentration of each standard was estimated considering with the MMA contraction. The polymerized standards were sliced 1 mm thick and observed by XSAM under the same conditions as implanted specimens.

TABLE I. Organometallic Compounds Used for Standard Specimens

Element	Compound
P	Tryphenylphosphine[a]
S	Sodium N,N-diethyldithiocarbamate tryhydrate[a]
Ca	Calcium chloride[a]
Cr	$Tris$(2,4-pentanedionato) chromium (III)[b]
Mn	$Tris$(2,4-pentanedionato) manganese(III)[b]
Fe	Dycyclopentadienyliron(II)[a]
Ni	Nickel(II) acetylacetonate, dyhydrate[a]
Cu	Copper(II) acetylacetonate[a]
Zn	Bis(2,4-pentanedionato) zinc(II)[b]

[a] Kanto Kagaku (Tokyo, Japan).

[b] Dojindo (Kumamoto, Japan).

Preparation of Standard Specimens with Borate Glass Matrix

The high concentration standard was prepared with lithium borate glass. Various amounts of Fe_2O_3, Cu_2O, and $Ca(OH)_2$ were mixed into 10 wt % Li_2O-B_2O_3 glass. The mixture was melted at 1000°C for 2 h in air using an alumina crucible and poured onto a brass plate. The poured melt was quenched by pressing with another brass plate to obtain a glassy solid 1 mm thick. The cooled glass was crushed into small pieces. The pieces of standards were set on an acryl plate and analyzed with XSAM.

XSAM Observation of Standard Specimens and Metal-Implanted Soft Tissue

XSAM observation was carried with the incident X rays generated from an Rh anode under conditions of 50 kV and 1 mA. X-ray irradiation was done using an X-ray guide tube (XGT) 100 mmϕ in diameter. The stage scanning was repeated in air 100 times for about 3 days and the mapping image was integrated. The average X-ray intensity from the standard specimens was estimated from the average brightness of the mapping image.

The implant materials consisted of 99.9% Cu, 99.9% Ni, and 99.5% Fe wires (1 mmϕ × 10 mm). The procedure of implantation and preparation of specimens was described elsewhere.[3] The resin-embedded tissue blocks were sliced 1 mm thick, polished with alumina emulsion, and emloyed for XSAM observation. Calibration curves of $K\alpha$ peak intensity and the concentration of each element were made using standards.

RESULTS

Figure 1 shows the Mn, Zn, and Cr mapping images of resin-based standard specimens. The brightness of Mn and Cr standards increased with the concentration. The relationship between the fluorescence X-ray intensity and the brightness is provided by the contrast bar at the bottom of photograph.
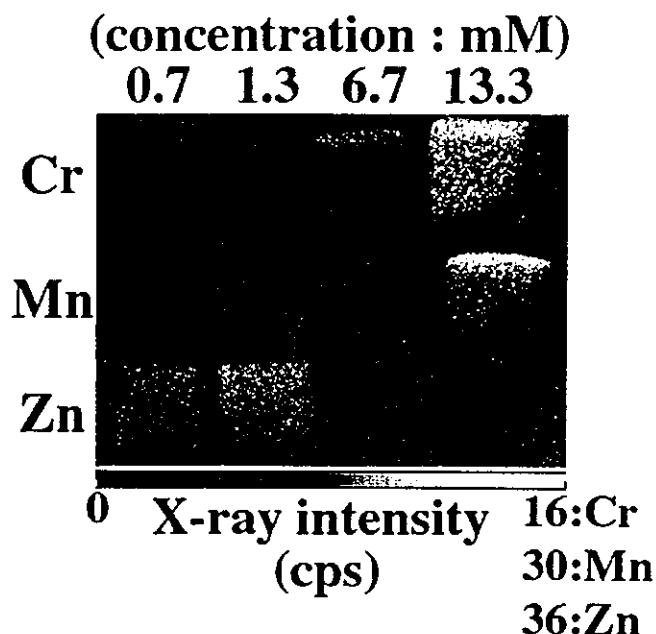

Figure 1. XSAM mapping images of Mn, Zn, and Cr standard specimens.

From the brightness of each standard specimen and the contrast bar, the calibration curve could be estimated.

The estimated calibration curves are shown in Figures 2, 3, and 4. Figure 2 shows the relationship between the fluorescent X-ray intensities of P, S, and Ca and their concentrations in an MMA matrix. The concentration range of Ca standard was restricted to low concentration due to the low solubilities less than 3 mM of calcium chloride in HEMA. The X-ray intensity of S slightly increased with increase in the S concentration. That of P showed a nonlinear increase with regard to the P concentration. It was considered to be due to the self-absorption of fluorescent X-rays by P itself.
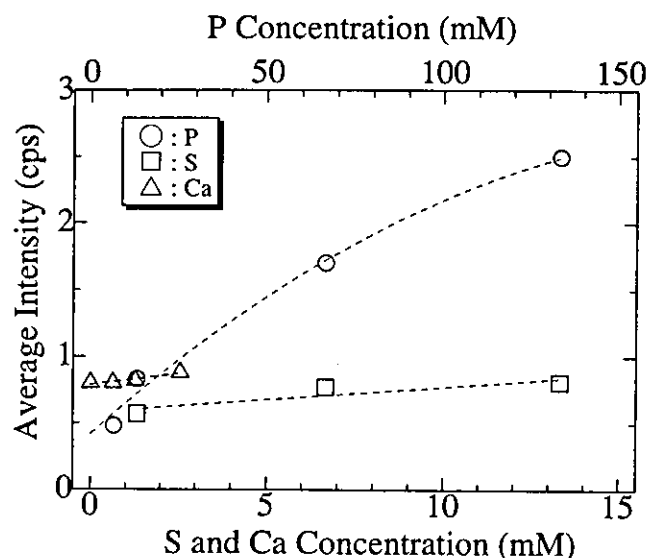

Figure 2. Relationships between the fluorescent X-ray intensities of P, S, and Ca and their concentrations in MMA resin matrix.
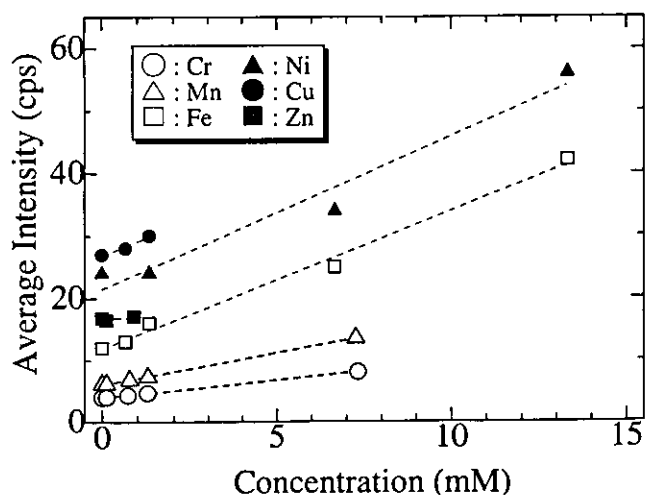
Figure 3. Relationships between the fluorescent X-ray intensities of Cr, Mn, Fe, Ni, Cu, and Zn and their concentration in MMA matrix.

Figure 3 shows the relationships between the fluorescent X-ray intensities of the metallic elements (Cr, Mn, Fe, Ni, Cu, and Zn) and their concentrations in the MMA matrix. The concentration ranges of Cu and Zn were restricted to low concentrations due to the low solubilities less than 1 mM of copper acetylacetonate and bis(2,4-pentanedionato) zinc in MMA. For four other elements—Cr, Mn, Fe, and Ni—their organic compounds showed relatively good solubility in MMA and linear relationships between the fluorescent X-ray intensities and their concentrations in an MMA matrix were obtained.

Figure 4 shows the relationships between the fluorescent X-ray intensities of Ca, Fe, and Cu and their concentrations in the lithium borate glass matrix as the high-concentration standards. Each specimen was transparent and no crystallization was observed. This indicated that the lithium borate glass showed the high solubility of Ca, Fe, and Cu oxide and high-concentration standards were successfully prepared. Linear relationships were observed for Ca, Cu, and the low-
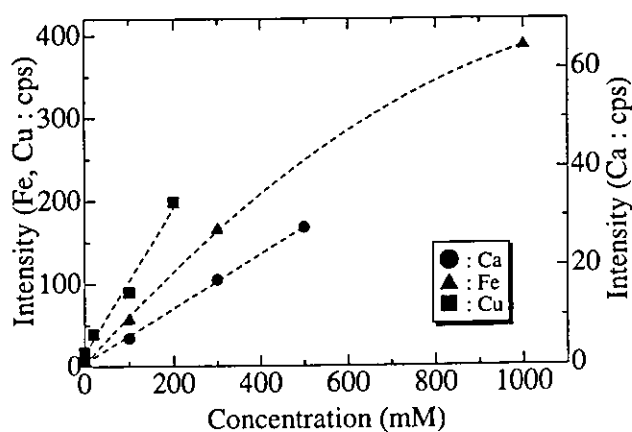

Figure 4. Relationships between the fluorescent X-ray intensities of Ca, Fe, and Cu and their concentrations in lithium borate glass matrix.
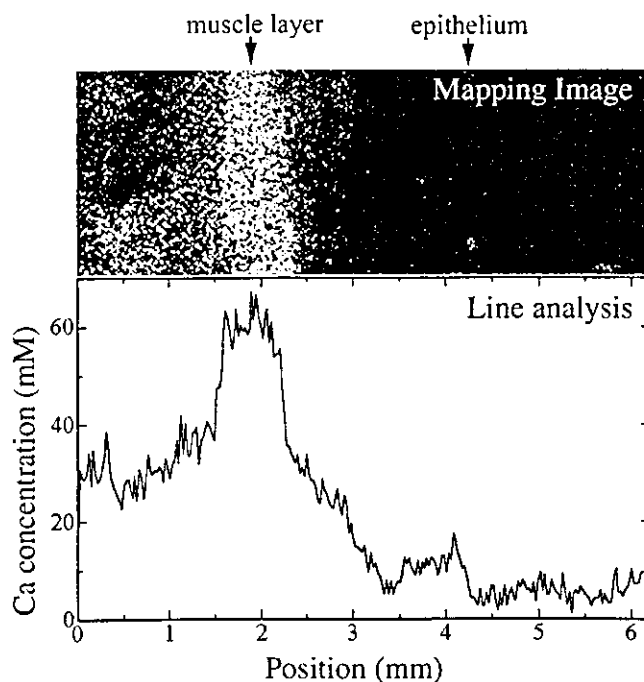

Figure 5. Ca distribution image of rat soft tissue and estimated Ca concentration in line analysis.

concentration range of Fe. In the high-concentration range of Fe, a nonlinear relationship was observed. It was considered to be due to the self-absorption of fluorescent X rays by Fe itself.

Figure 5 shows the Ca distribution in the rat subcutaneous layer and the estimated concentration using the Ca standard specimen. The Ca concentration in the rat subcutaneous tissue is higher than the range of resin-based Ca standard (Figure 3); therefore, the borate glass-based Ca standard (Figure 4) was used for the estimation. The highest Ca concentration in the rat subcutaneous tissue was estimated to be 60 mM at the muscle layer.

Figure 6 shows the elemental distribution around the Fe, Cu, and Ni implants by XSAM elemental mapping. The implants were placed in the center of observed areas. Clear dissolution of the metallic element was observed around the implants in the mapping images. Figure 7 shows the line analysis of Cu, Ni, and Fe mapping images shown in Figure 6 using the standards of Ni (Figure 3) and Cu and Fe (Figure 4). Fe had an extremely high concentration around the implant, estimated to be 1000 mM. The maximum concentrations of Cu and Ni were estimated to be 40 and 20 mM, respectively.

DISCUSSION

In this study, the standards for XSAM were prepared using organometallic compounds dissolved in MMA resin and metal oxides dissolved in lithium borate glass. The tissue specimens were embedded in MMA. Therefore, the MMA-
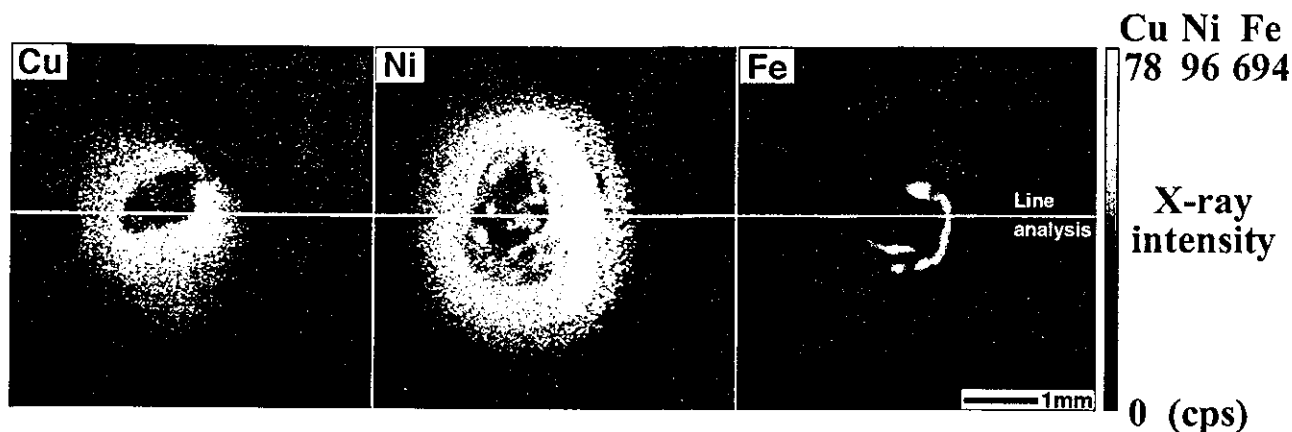
Figure 6. Elemental distribution image around the Fe, Ni, and Cu implants in rat soft tissue.

based standard was desirable. However, the species and concentration ranges of standards were limited because of the low solubility of metal organic compounds in MMA. Therefore, standard specimens with wider concentration ranges were prepared using a glass matrix. A glass matrix usually has wide solubility for various metallic oxides. For the use of the XSAM standard, low X-ray absorption is required. The lithium borate matrix consisted of light element cations and low absorption was expected. The mass absorption coefficient of 10 wt % Li_2O-B_2O_3 glass was estimated to be $36(cm^2/g)$ for the X-ray of 6.4 keV from the mass absorption rate of the contained elements.[8] This coefficient is higher than that of MMA resin (14 cm^2/g) but much lower than SiO_2 (77 cm^2/g), which is the base component of ordinary glass. Therefore, lithium borate glass was considered an appropriate

matrix for the XSAM standard. Figures 2, 3, and 4 show the relationships between the fluorescent X-ray intensities of elements and their concentrations in MMA- and glass-based matrices. The increment of the X-ray intensity for the concentration of each element shows the XSAM sensitivity of the element. As shown in Figure 8, the sensitivity increased with the atomic number of element. This tendency means that XSAM shows higher sensitivity for heavier elements.

The authors reported that the Ca, P, and S distribution in rat soft tissue could be visualized using XSAM.[4] Using the results in Figure 2, the P concentration in the rat skin could be estimated as approximately $10mM$ (0.03 wt %). The S and Ca concentrations in soft tissue were outside of the range of the MMA-based standard specimens. In a previous article,[2] the authors could estimate the concentration of dissolved Ni in rat
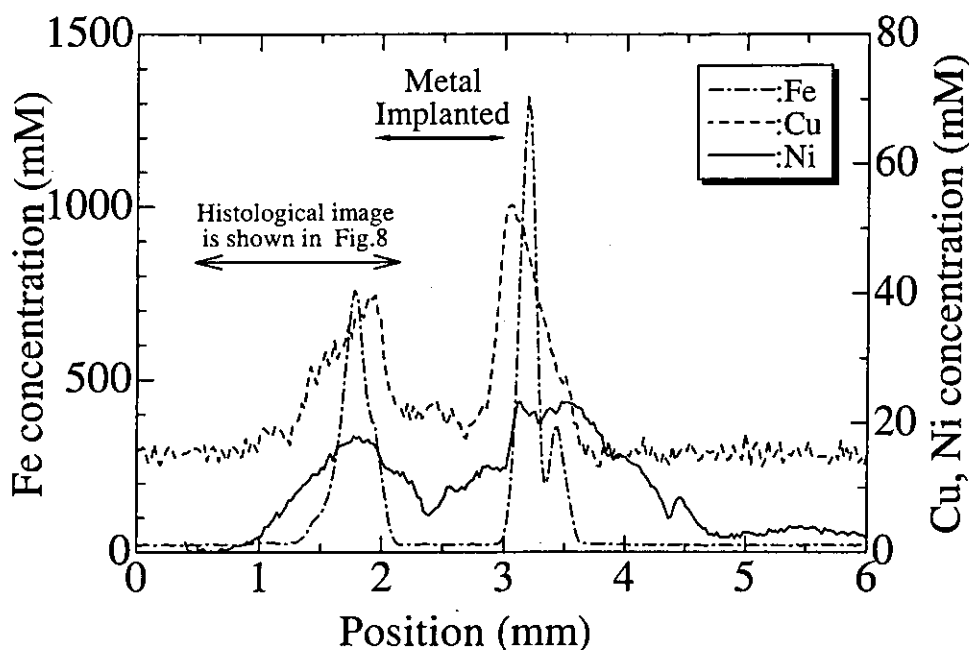

Figure 7. Dissolved Fe, Ni, and Cu concentration curves around implants (along the white line shown in Figure 6).

soft tissue from implanted Ni. However, the other elements, for example, dissolved Cu and Fe in the soft tissue from these implants and Ca in rat soft tissue, were outside of the range of the MMA-based standards. Therefore, borate glass-based standards with high contents of the elements were developed and the concentrations in soft tissue could be estimated as shown in Figures 5 and 7. In Figure 5, the estimated Ca concentration in the rat muscle is approximately 60 mM (0.2 wt %). The Ca concentration is reported to be typically 0.006 wt % in rat skeletal muscle. The estimated Ca concentration in this article was more than 10 times higher than the reported value. Shrinkage during specimen preparation and MMA resin condensation would be one reason for this difference.

The dissolution of metallic elements from pure metal implants was also estimated as shown in Figure 7. Fe showed a much higher concentration around the implant, estimated as 1000 mM, than Cu and Ni. Figure 9 shows histological tissue images with low magnification around the implants in the area shown in Figure 7. Severe tissue degradation was observed around Cu and Ni implants, whereas relatively moderate tissue damage was observed around the Fe implant. In a previous article,[3] severe inflammatory responses such as necrosis of cells, emigration of macrophages, and dilation of blood vessels were observed around the Ni and Cu implants in histological observation at high magnification. The Cu implant was encapsulated in a cystic structure and the inside of the cystic structure was filled with a blue exudate. The exudate was lost during specimen processing. Therefore, the original concentration of Cu was considered to be higher than the present concentration. Considering the severe inflammatory response around the Ni implant and the low dissolved
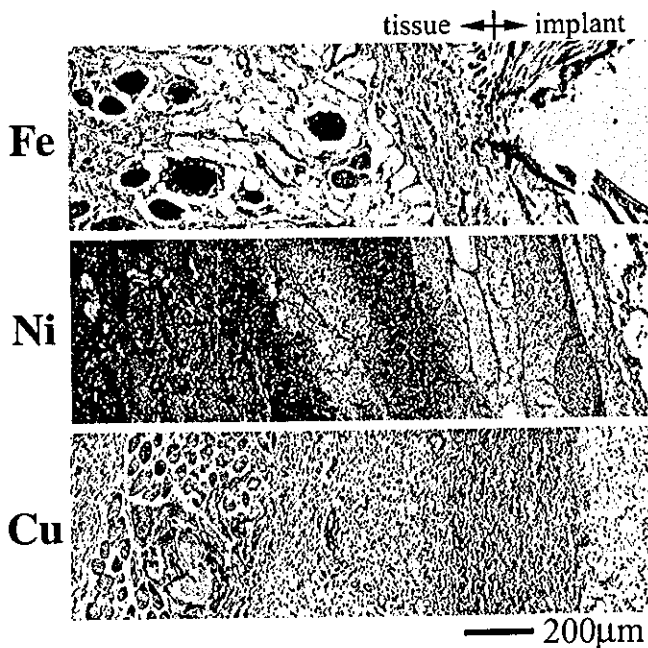

Figure 8. Experimentally obtained dependence of fluorescent X-ray sensitivity on the atomic number.
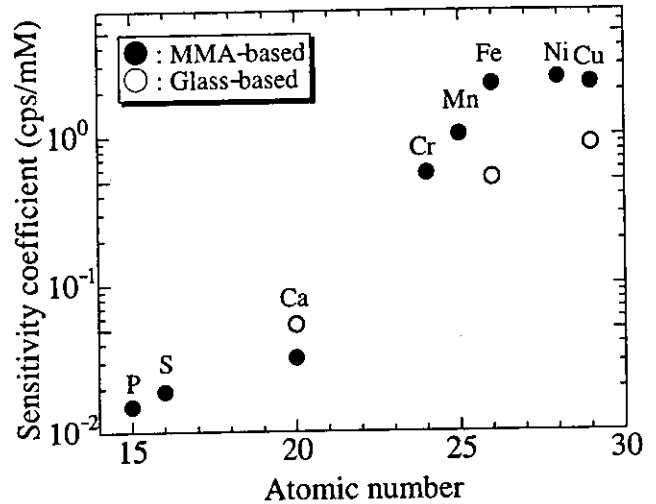

Figure 9. Histological images of the Fe-, Ni-, and Cu-implanted tissues.

concentration, the high toxicity of Ni for soft tissue was confirmed. The toxicity of Cu was estimated to be less than that of Ni but both showed high toxicity even at a low concentration such as 10 mM. In contrast, Fe was not as toxic as Ni and Cu even at the high concentration of 1000 mM.

CONCLUSIONS

For XSAM quantitative analysis of various elements dissolved in soft tissues, two different types of standard specimens, MMA based and borate glass based, were prepared for P, S, Ca, Cr, Mn, Fe, Ni, Cu, and Zn. The solubility of metal organic compounds in MMA was low. Therefore, the low-concentration standard specimens were made with the MMA base. In contrast, the borate glass matrix usually has wide solubility for various metallic oxides and the standard specimens for higher concentrations were made with the glass base. Using these standard specimens, the P and Ca concentrations in rat normal tissue and dissolved Ni, Fe, and Ni concentrations in metal-implanted tissues were quantitatively analyzed. The estimated concentrations of dissolved Fe, Cu, and Ni were 1000, 40, and 20 mM, respectively. From the concentration level that caused inflammation around the implants, the high toxicity of Ni for soft tissue was confirmed. The toxicity of Cu was estimated as slightly less than that of Ni. In contrast, Fe showed low toxicity despite a concentration of dissolved Fe as high as 1000 mM.

In this study, various standard specimens were developed for soft-tissue analysis by XSAM and it was possible to quantitatively analyze various elements dispersed in soft tissue. In particular, the metallic element with low concentrations could be quantitated by XSAM and the relationship between the concentration and tissue reaction estimated.

REFERENCES

1. Hosokawa Y, Ozawa S, Nakazawa H, Nakayama Y. An X-ray guide tube and a desk-top scanning X-ray analytical microscope. X-Ray Spectrom 1997;26:380–387.
2. Uo M, Watari F, Yokoyama A, Matsuno H, Kawasaki T. Dissolution of nickel and tissue response observed by X-ray scanning analytical microscope. Biomaterials 1999;20:747–755.
3. Uo M, Watari F, Yokoyama A, Matsuno H, Kawasaki T. Tissue reaction around metal implants observed by X-ray scanning analytical microscopy. Biomaterials 2001;22:677–685.
4. Uo M, Watari F, Yokoyama A, Matsuno H, Kawasaki T. Visualization and detectability of elements rarely contained in soft tissue by X-ray scanning analytical microscopy and electron-probe micro analysis. Biomaterials 2001;22:1787–1794.
5. Xu S, Kitajo H, Kawashima I, Yamane Y, Murata M, Shibata T, Arisue M, Endo K, Shi S, Ohno H. X-ray scanning analytical microscopic and scanning electron microscopic studies of an unusual case of dens invaginatus. Higashi Nippon Dent J, 2000; 19:143–157.
6. Uo M, Watari F. Rapid analysis of analysis of metallic dental restoratives using X-ray scanning analytical microscopy. Submitted for publication.
7. Roomans GM, Van Gaal HLM. Organometallic and organometalloid compounds as standards for microprobe analysis of epoxy resin embedded tissue. J Microsc 1977;109:235–240.
8. Weast RC, editor. CRC handbook of chemistry and physics, 69th ed. Boca Raton, FL: CRC Press; 1988–1989. p E144–147.

Rare Earth Oxide-containing Fluorescent Glass Filler for Composite Resin

Motohiro UO[1], Mayumi OKAMOTO[2], Fumio WATARI[1], Kazutoshi TANI[3], Manabu MORITA[3] and Akira SHINTANI[4]

[1]Division of Biomedical, Dental Materials and Engineering, Department of Oral Health Science, Graduate School of Dental Medicine, Hokkaido University, North 13 West 7, Kita-ku, Sapporo 060, Japan

[2]Division of Oral Functional Prosthodontics, Department of Oral Functional Science, Graduate School of Dental Medicine, Hokkaido University, North 13 West 7, Kita-ku, Sapporo 060, Japan

[3]Division of Preventive Dentistry, Department of Oral Health Science, Graduate School of Dental Medicine, Hokkaido University, North 13 West 7, Kita-ku, Sapporo 060, Japan

[4]OptoElectronics Department, Toyoda Gosei Co. Ltd. (Present address: Koha Co. Ltd.)

Corresponding author, E-mail: uo@den.hokudai.ac.jp

In recent dental care, esthetic restorative materials such as composite resin and porcelain have been widely used and studied. However, their good esthetics makes the visual inspection of restored teeth difficult. In this study, a fluorescent glass filler containing rare earth oxides — which are well-known fluorescent materials — was prepared and used in composite resin to enhance visual inspection capability with small change in color. For example, when irradiated with near ultraviolet light, an Eu_2O_3-containing filler fluoresced clearly and visibly. The fluorescence intensity of the prepared composite resin increased with increase of Eu_2O_3 content in the glass filler and with filler/resin ratio in the resin. Despite the clear fluorescence, the effect of Eu_2O_3 on the color change of composite resin was quite small — even when up to 10 wt% Eu_2O_3 was added to the glass filler. Tb_4O_7- and Dy_2O_3-added fillers also showed clear fluorescence, just like Eu_2O_3-added filler. Therefore, fluorescent glass fillers for composite resins, resulting in small color change in the latter, were successfully prepared in this study.

Key words: Rare earth oxide, Europium, Fluorescence, Filler, Composite resin

INTRODUCTION

In recent dental care, esthetics is of paramount importance to patients. Therefore, restorative materials such as composite resin and porcelain have been widely used and studied[1-8]. However, because of their good esthetics, the visual inspection of restored teeth becomes difficult. In particular, quick and accurate inspection in mass dental health examinations becomes increasingly difficult for dentists. This is because detection is usually done by exploring the tactile difference on the tooth surface. If the composite resin shows some distinct optical feature, then visual inspection of the restored part could be easily achieved. Fluorescence is a good property for use as a non-contact detection method for various materials. As such, it has already been applied in many fields[9-11]. In the current study, the authors applied the fluorescence detection method to discriminate between esthetic restoratives and teeth[12,13].

Rare earth oxides are well-known and widely-used fluorescent materials[14]. Silicate glass, which constitutes the glass filler of composite resin, provides good solubility for other oxides containing rare earth oxides. Leveraging on this solubility property, a rare earth oxide-containing glass filler could then fluoresce — making visual inspection possible.

The purpose of this study was to prepare a fluorescent glass filler for use in a composite resin to enhance visual inspection capability without change in color.

MATERIALS AND METHODS

Preparation of fluorescent glass filler

Glass was prepared by mixing reagent grade chemicals $Na_2B_4O_7$, B_2O_3, Al_2O_3, and SiO_2 to form $10Na_2O \cdot 49B_2O_3 \cdot 1Al_2O_3 \cdot 40SiO_2$ (wt%). Rare earth oxides (Eu_2O_3, Dy_2O_3, Tb_4O_7, Nd_2O_3, Ho_2O_3, Er_2O_3, and Sm_2O_3) were added to the above mixture at 2, 5, 7, and 10 wt%. The mixture was melted at 1100℃ for two hours in air using an alumina crucible. The melt was cast in a brass mold into a thin sheet, and quenched. The prepared glass was crushed and sieved to be under 53 μm, and supplied for composite resin preparation.

Preparation of composite resin

Urethanedimethacrylate (UDMA; Shin Nakamura Kagaku, Wakayama, Japan) was used as the resin matrix. Camphoroquinone (Tokyo Kasei, Tokyo, Japan) was added to UDMA at 0.3 wt% as a photocure catalyst. The prepared glass filler and UDMA were mixed at filler/resin weight ratios (f/r) of 1/1, 2/1, and 3/1. The mixture was put in a plastic mold (8-mm diameter × 2-mm thickness) and cured with a light curing unit (JetLight 3000, Morita, Tokyo, Japan) for 30 seconds from both sides. The cured

specimen was applied for optical measurement without polish.

Measurement of optical properties
One human third molar was sliced perpendicular to the tooth axis to expose the enamel, and then polished with $\phi 2 \mu m$ alumina slurry to expose the dentin. Their fluorescence spectra were measured using a fluorescence spectrophotometer (F-2500, Hitachi, Tokyo, Japan) under the following conditions: slit width=2.5 nm, wavelength scanning speed=300 nm/min. When irradiated by a purple light-emitting diode (purple-LED[#]; Toyoda Gosei Co. Ltd., Nakajima-gun, Aichi, Japan), the fluorescence image was observed and recorded with a digital camera (D60, Canon Co. Ltd., Tokyo, Japan). The camera was attached with a sharp cut filter (O56, Hoya Co. Ltd., Tokyo, Japan) to cut off irradiating light. The effect of Eu_2O_3 content — in the filler — on the color of composite resin was estimated with a color-difference meter (OFC-300A, Nihon Denshoku Kogyo Co. Ltd., Tokyo, Japan). For each condition, the fluorescent measurement and color estimation were carried out once for each specimen.

RESULTS

The excitation and emission spectra of 10 wt% Eu_2O_3-containing filler mixed at f/r=3/1 are shown in Fig. 1. Sharp peaks were observed in both the excitation and emission spectra. Strong excitation bands were distributed in the wavelengths below 400 nm and strong peaks were observed at 395 nm and 382 nm. As for the emission spectrum, strong peak was observed at around 613 nm.
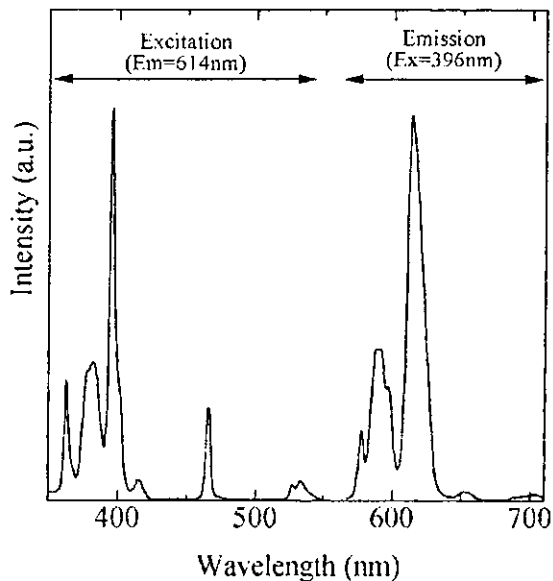
As shown in Fig. 2, the fluorescence intensity at 613 nm when excited at 396 nm was dependent on two factors: Eu_2O_3 content in the glass filler and filler/resin ratio (f/r). Fluorescence intensity increased with increase in both the Eu_2O_3 content and filler/resin ratio. Each intensity curve was saturated with increase in Eu_2O_3 content in the glass filler. This was caused by self-absorption or concentration quenching of fluorescence. At 5 wt% Eu_2O_3 filler and f/r=2/1, more than 50% of maximum emission (*i.e.*, 10 wt% Eu_2O_3 filler and f/r=3/1) was already achieved.

The fluorescence image of Eu_2O_3-containing composite under purple-LED (383 nm) irradiation is shown in Fig. 3. For comparison purpose, a conventional commercial composite (Vita Shade, 3M) was also shown in the figure. A clear fluorescence visibly emitted from the Eu_2O_3-containing composite, where the composite could be easily identified by the fluorescence through macroscopic observation. By contrast, the commercial composite did not show clear fluorescence under the same irradiation conditions.
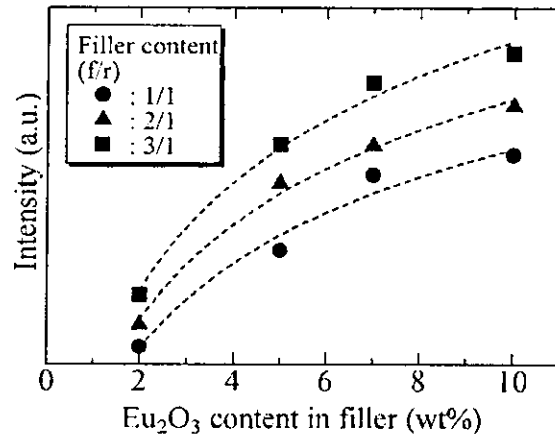

Fig. 2   The dependency of fluorescence intensity (at 613 nm under excitation at 396 nm) on filler/ resin ratio (f/r) and Eu_2O_3 content in glass filler.
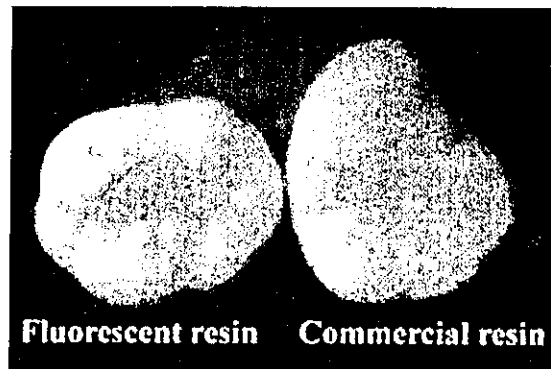

Fig. 3   The fluorescence image of Eu_2O_3-containing composite under purple LED (383 nm) irradiation.

Fig. 1   The excitation and emission spectra of 10 wt% Eu_2O_3-containing filler mixed at f/r=3/1.

The effect of Eu_2O_3 addition — to the filler — on the color change of composites is shown in Table 1. At f/r=2/1, Table 1 shows the L^*, a^*, and b^* parameters of the CIE color system for composites with Eu_2O_3-containing fillers and filler without Eu_2O_3. The effect of Eu_2O_3 content on color change was very small, such that any difference in color among the composites was not distinctly visible to the eye. Therefore, the effect of Eu_2O_3 on the color change of composite resin was negligible.

Fig. 4 shows the emission spectra of Eu_2O_3-containing composite, enamel, and dentin under exci-

Table 1   The effect of Eu_2O_3 content on color of composites (at f/r=2/1)

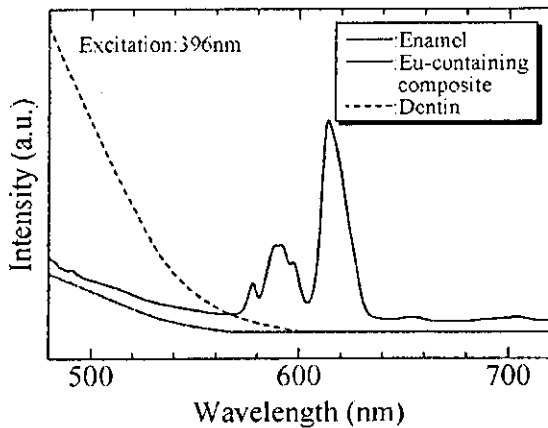| Eu content (%)	L^*	a^*	b^*
0	50.6	−1.0	1.0
5	49.6	−0.7	1.4
10	52.3	−1.0	2.2

Fig. 4   The emission spectra of Eu_2O_3-containing composite, enamel, and dentin under excitation at 396 nm.
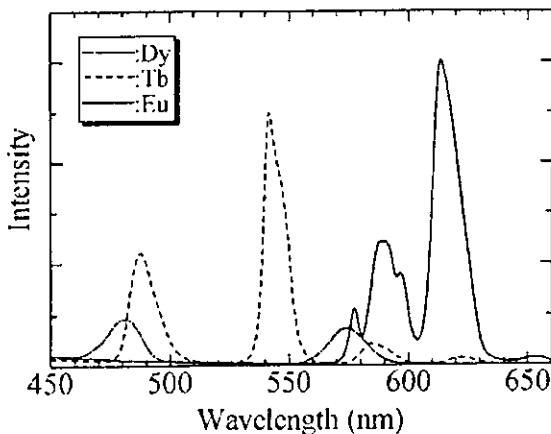

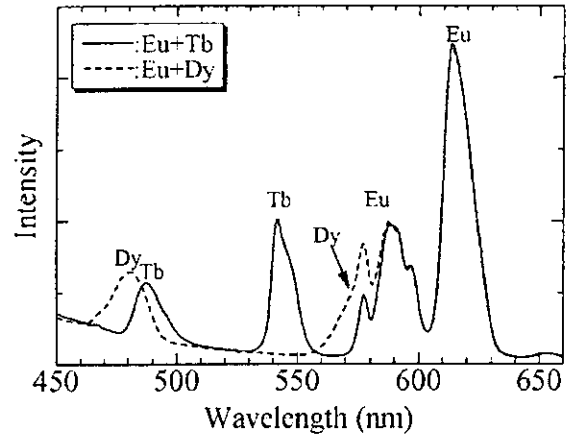Fig. 5   The emission spectra of the composites with Tb_4O_7- and Dy_2O_3-containing fillers (10 wt%).

Fig. 6   The emission spectra of the composites with Eu_2O_3/ Tb_4O_7 or Eu_2O_3/Dy_2O_3.

tation at 396 nm. The Eu_2O_3-containing composite showed higher emission intensity than enamel within the observed wavelength range. Dentin had higher emission intensity at wavelengths shorter than 560 nm, while Eu_2O_3-containing composite showed higher emission intensity at wavelengths longer than 560 nm. By using an appropriate filter to pass wavelengths longer than 560 nm, the emission of Eu_2O_3-containing composite could be clearly differentiated from dentin.

Fig. 5 shows the emission spectra of the composites containing fillers with Tb_4O_7 and Dy_2O_3 (10 wt%). Both Tb_4O_7 and Dy_2O_3 showed clear emissions, but not so for composites that contained other rare earth oxides. Fig. 6 shows the emission spectra of composites with both Eu_2O_3 and Tb_4O_7 or Dy_2O_3 (5 wt% respectively). The emissions from Eu, Tb, and Dy were easily identified and assigned.

DISCUSSION

Due to the recent improvement of esthetic restorative materials such as composite resin and porcelain, greater skills are now required of dentists to detect resin-filled teeth. As shown in Fig. 3, an Eu_2O_3-containing glass filler lent a strong fluorescent property to the composite resin when the latter was irradiated by purple or near ultraviolet light. The fluorescence could be observed visually. Further, as shown in Table 1, the addition of Eu_2O_3 did not affect the color of composite resin. This meant that the effect of Eu_2O_3 content on the color change of composite resin was negligibly small.

As for the light source, a purple or near ultraviolet LED was used. Compared to conventional light sources, these LED light sources wielded several advantages: small in size, sharp emission spectrum, and low electricity consumption. And these advantages were the reasons that made LED an appropri-

ate inspection device in the oral cavity.

The authors have studied the discrimination of esthetic restorative materials based on their fluorescent properties[12,13]. Most commercial porcelains and composite resins show typical fluorescence at the longer wavelengths when irradiated by blue light. Therefore, the possibility of non-contact discrimination of these materials was suggested. To confirm this possibility, the present study designed an easy and clear method to discriminate between composite resin and tooth using rare earth oxides — which could likewise be applied to porcelains.

As shown in Figs. 5 and 6. Tb_4O_7- and Dy_2O_3-containing composite resins also showed clear fluorescence, just like Eu_2O_3, and their emissions also easily assigned. This indicated the possibility of systematic recording of data when the combination and/or composition of these rare earth oxide-containing glass fillers were changed. For example, in the current study, the presence (or absence) of the three rare earth oxides could be expressed as three bits of data. If a glass filler contained Er and Tb but without Dy, the expression could be assigned as (1,1,0). By including the composition of rare earth oxide in the filler as a parameter, more information could be expressed. Thus, with this method, it would be possible to systematically record information on rare earth oxide-containing glass fillers — apart from product information such as lot number.

CONCLUSIONS

In this study, we developed a fluorescent glass filler which induced a small color change in composite resins. We then used it in a composite resin to enhance the latter's visual inspection capability. The Eu_2O_3-containing filler fluoresced clearly and visibly when irradiated with purple or near ultraviolet light. Fluorescence intensity of the prepared composite resin increased with increase of Eu_2O_3 content in the glass filler and with filler/resin ratio in the resin. Nevertheless, addition of up to 10 wt% Eu_2O_3 to the glass filler did not change the color of the composite resin. Tb_4O_7- and Dy_2O_3-added fillers also showed clear fluorescence. The emissions of Eu_2O_3, Tb_4O_7. and Dy_2O_3 were characteristic of these elements, and hence easily identified and assigned in the spectra. Therefore, in the present study, fluorescent glass fillers for composite resins were successfully prepared — where color change in composite resin was negligibly small and that the possibility of systematic data recording was also suggested.

ACKNOWLEDGEMENTS

REFERENCES

1) Bello A, Jarvis RH. A review of esthetic alternatives for the restoration of anterior teeth. J Prosthet Dent 1997; 78: 437-440.

2) van Dijken JWV. Direct resin composite inlays/onlays: An 11-year follow-up. J Dent 2000; 28: 299-306.

3) Arikawa H, Kanie T, Fujii K, Homma T, Takahashi H, Ban S. Optical properties of paint-on resins for shade modification of crown and bridge resins — Light transmittance characteristics. Dent Mater J 2003; 22: 272-279.

4) Soma H, Miyagawa Y, Ogura H. Setting and flexural properties of metal-resin composite using Ag-Cu particles as filler and chemical accelerator. Dent Mater J 2003; 22: 543-555.

5) Bayindir YZ, Yildiz M, Bayindir F. The effect of "soft-start polymerization" on surface hardness of two packable composites. Dent Mater J 2003; 22: 610-616.

6) Arksornnukit M, Takahashi H, Nishiyama N. Effects of silane coupling agent amount on mechanical properties and hydrolytic durability of composite resin after hot water storage. Dent Mater J 2004; 23: 31-36.

7) Tjandrawinata R, Irie M, Yoshida Y, Suzuki K. Effect of adding spherical silica filler on physico-mechanical properties of resin modified glass-ionomer cement. Dent Mater J 2004; 23: 146-154.

8) Arikawa H, Kanie T, Fujii K, Ban S, Homma T, Takahashi H. Optical and color stabilities of paint-on resins for shade modification of restorative resins. Dent Mater J 2004; 23: 155-160.

9) Matsumoto H, Kitamura S, Araki T. Applications of fluorescence microscopy to studies of dental hard tissue. Front Med Biol Eng 2001;10: 269-284.

10) Fujikawa K, Sugawara A, Kusama K, Nishiyama M, Murai S, Takagi S, Chow LC. Fluorescent labeling analysis and electron probe microanalysis for alveolar ridge augmentation using calcium phosphate cement. Dent Mater J 2002; 21: 296-305.

11) Shigetani Y, Okamoto A, Abu-bakr N, Tanabe K, Kondo S, Iwaku M. Caries diagnosis sing a laser fluorescence system — Observation of autofluorescence of dental caries. Dent Mater J 2003; 22: 56-65.

12) Tani K, Watari F, Uo M, Morita M. Discrimination between composite resin and teeth using fluorescence properties. Dent Mater J 2003; 22: 569-580.

13) Tani K, Watari F, Uo M, Morita M. Fluorescent properties of porcelain-restored teeth and their discrimination. Mater Trans 2004; 45: 1010-1014.

14) Tanabe S. Kidorui no Kagaku (Adachi G ed.), Kagaku Dojin, Kyoto, 1999, pp.775-811.

The first observation of carbon nanotubes by spherical aberration corrected high-resolution transmission electron microscopy

Nobuo Tanaka[1], Jun Yamasaki, Tomoyuki Kawai and Huayong Pan

EcoTopia Science Institute and Department of Crystalline Materials Science,
Nagoya University, Chikusa-ku, Nagoya 464-8603, Japan

E-mail: a41263a@nucc.cc.nagoya-u.ac.jp (N Tanaka)

Abstract

High-resolution transmission electron microscopy (HRTEM) of multi-wall
carbon nanotubes using a spherical aberration correction of the objective
lens has shown a new possibility for the observation of nanometre-sized
tubular materials. Improvement of the image resolution along a direction
parallel to that of electron incidence enables one to obtain some information
on the local height of the tubes, and in lateral directions better than 0.14 nm
at 200 kV accelerating voltage, the possibility of direct determination of the
chirality of the tubes and the observation of finer atomic structures of carbon
atoms such as 'hexagon' ones is suggested. Spherical aberration corrected
HRTEM begins a new stage of the structural study of nano-tubular materials.

1. Introduction

New kinds of imaging techniques down to 0.1 nm spatial
resolution have been recently developed in transmission
electron microscopy. One is annular dark field scanning
transmission electron microscopy (ADF-STEM) [1], and
another is spherical aberration corrected transmission electron
microscopy (C_s-corrected TEM) [2]; these enable one to obtain
a more directly interpretable image contrast up to about 0.1 nm
even using instruments of 200 kV accelerating voltage. In
the present study carbon nanotubes are observed for the first
time with a newly developed 200 kV C_s-corrected TEM in
order to study the imaging characteristics of the TEM and
its effective application of nano-structured materials [3, 4],
rather than bulk crystals [5]. One of the remaining issues
for high-resolution electron microscopy of carbon nanotubes
is to see the atomic arrangements of the side wall in order
to determine their chirality by electron microscopy, similarly
to scanning tunnelling microscopy [6], or to obtain three-

dimensional information of the tubes, such as the configuration
and conformation. In this paper we discuss the possibilities
mainly of the former issue, but partly of the latter one by using
actual high-resolution TEM images and the corresponding
simulated ones.

2. Methods

2.1. Electron microscopy

A C_s-corrected HRTEM was newly developed using a 200 kV
conventional thermal field-emission HRTEM (JEOL:JEM-
2010F [7] and 2100F). The spherical and chromatic aberration
coefficients (C_s and C_c) of the non-corrected objective lens
were 0.5 and 1.1 mm, respectively [8]. The C_s-correction
was made electron-optically by two additional hexapole
correctors positioned below the objective lens as well as
transfer doublet lenses, which were developed by Rose and
Haider several years ago [2]. *In situ* and accurate measurement
of optical parameters, such as the amount of defocus and up
to third-order aberration coefficients (C_1 (=Δf), C_3 (=C_s),

---

[1] Author to whom any correspondence should be addressed.

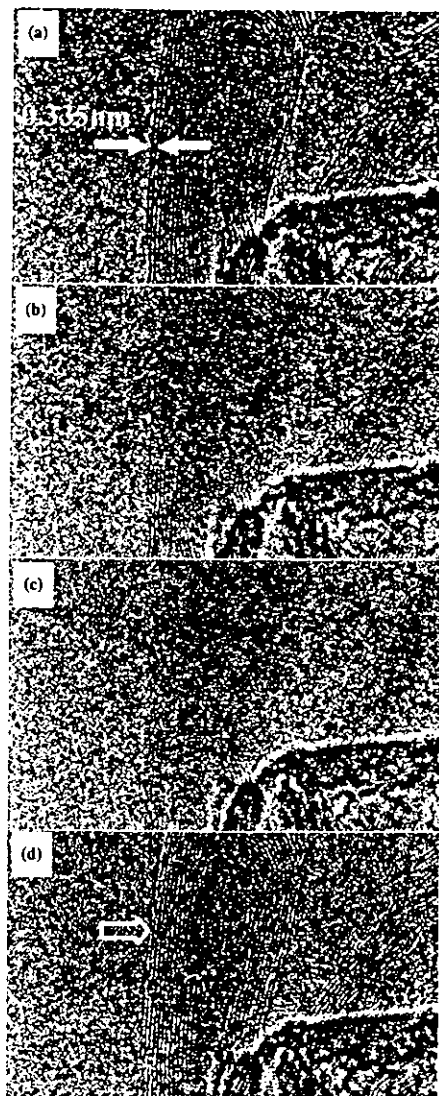Figure 1. Through-focus images of a multi-wall carbon nanotube (MWCNT) taken with a 200 kV spherical aberration corrected TEM.
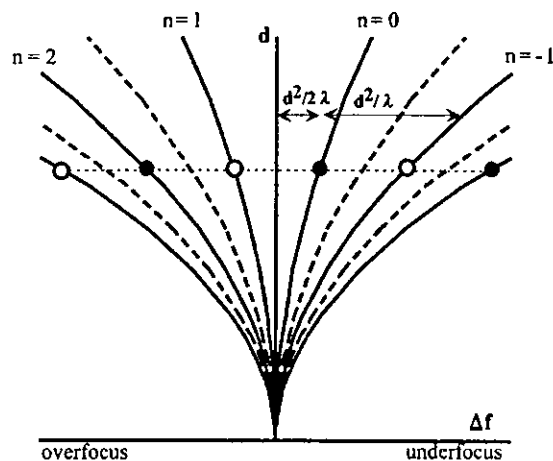

Figure 2. Imaging condition of a weak phase object for zero spherical aberration based on Fourier image theory as illustrated in Thon's diagram [14]. The vertical line denotes the spacing imaged (d), and the horizontal line the amount of defocus ($\Delta f > 0$; underfocus).

software for electron microscopy (Digital-Micrograph) and commercially based image software (PhotoShop).

Image simulations were performed for C_s-corrected HREM images with small and positive C_s-values by using a multi-slice program (MacHREM) with the correct consideration of tilted electron incidence with respect to sample crystals [11].

2.2. Sample preparation

The multi-wall carbon nanotubes (MWCNT) observed in the present study were prepared by an ordinary glow-discharge method from a carbon rod including transition metal catalysis [12]. The product was ground in an agate mortar with ethanol and dropped onto a holey carbon film on a copper grid.

3. Results and discussion

3.1. Improvement of image resolution along the electron incidence direction

A_1 (=astigmatism), B_2 (=coma) etc) of the objective lens, was successfully performed using a well-known Zemlin tableaux [9] with the incident beam tilted up to 18 mrad from the optical axis. Correction of the parameters into the optimum values was then made automatically using a LINUX computer monitored through a GUI in a WINDOWS computer. In the present study we have chosen C_s-values of +10 or 15 μm, which is one sixtieth the size of ordinary values such as 1 mm. The reason for the selection of a small but finite value is that if $C_s = 0$, the phase contrast of thin samples should be zero at the Gaussian focus [10]. It is noted that the value of C_c increases 1.45 mm from 1.1 mm after the C_s-correction [8]. Twenty or thirty through-focus images were taken across the in-focus condition with a defocus step of 2 nm. The images were recorded mainly using a high-sensitivity CCD camera of $1k \times 1k$ pixels (Tiez: F114). The digital images in this paper were manipulated, including Fourier filtering, with dedicated

Figure 1 shows through-focus images of a multi-wall carbon nanotube (MWCNT) taken near just-focus with the present C_s-corrected TEM. Lattice fringes of graphite (00,2) planes with spacing of 0.335 nm are clearly observed even near the in-focus condition. This is because the imaging condition of the lattice fringes is almost described by the Fourier image theory [13], as illustrated in figure 2, due to the very small C_s-values such as 15 μm. The lattice fringes are imaged with a high contrast at defoci, $+d^2/2\lambda$ (black contrast), $-d^2/2\lambda$ (white contrast), which amount to +22.3 nm for (00,2) planes of graphite, as calculated later. With a minimized Fresnel diffraction effect due to the small amount of defoci for observing the lattice fringes, the details of the side edge of the cylindrical tube are clearly identified, as indicated by a white open arrow in figure 1(d). This is one of the advantages of C_s TEM.

The phase contrast of the lattice images disappears at just-focus, as shown in figure 1(c). In this figure, the tiny speckle
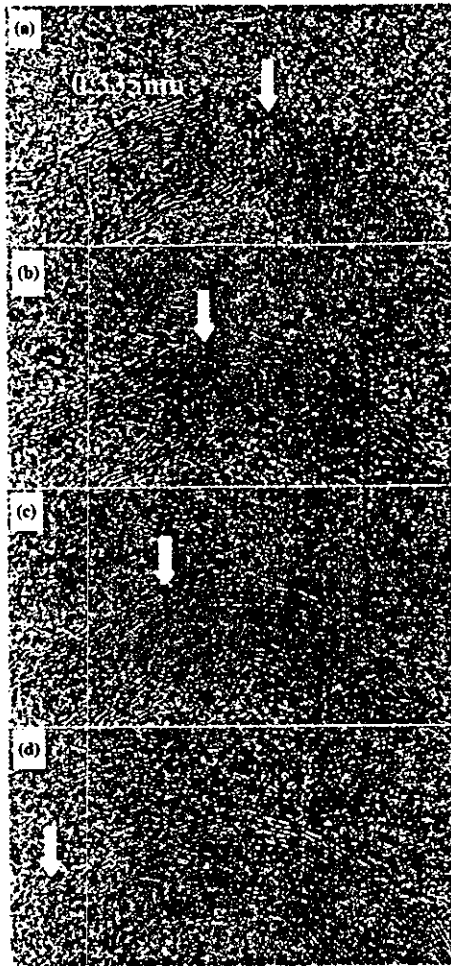
Figure 3. Similar through-focus images showing the movement of an area without (00,2) lattice fringes along an axis of a carbon nanotube.
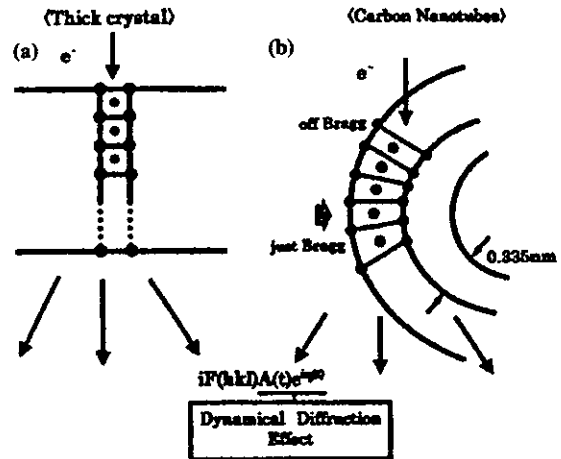

Figure 4. Schematic cross-sectional views of a perfect crystal like silicon (a) and a carbon nanotube (b), and the diffraction processes inside the samples.

patterns come from the quantum noise of the CCD camera used for image recording. In the lower part of the tube (in figure 1(c)), a faint contrast of lattice images is observed, which is caused by a slight difference in the height of the tube along the electron incidence direction (difference in z-position) as discussed later. This perfect disappearance of the fringes is easily understood using Thon's diagram [14, 15] with $C_s = 0$, as shown in figure 2. In the case of $C_s = 0$, parabolic curves start almost from the origin corresponding to Δf (defocus) $= 0$ and d (spacing) $= 0$. The vertical axis at $\Delta f = 0$ corresponds to an imaging condition giving no phase contrast for weak-phase objects. The curves of $n = 0$ and 1 correspond to black contrast and white contrast for single atoms, respectively, which are derived from the well-known contrast theory of weak-phase objects [10]. The broken curves in the figure give no phase contrast.

When a carbon nanotube is slightly tilted from normal to electron incidence, an area with no lattice fringe contrast moves along the nanotube depending on the height difference. Figure 3 shows through-focus images of another slightly tilted tube. The area indicated by the open arrow shows the disappearance of lattice fringes of 0.335 nm spacing. By

changing the amount of defocus from figures 3(a) to (d), the area moves along the nanotube axis. This is a kind of null-balance method in physical measurement. The focus width of disappearance (w) is determined by half of the horizontal distance between $n = 0$ and 1 curves corresponding to the spacing (d), as shown in figure 2 [15]; the width amounts to $w = d^2/2\lambda$. As the lattice spacing decreases, the width becomes small. Substituting 0.335 nm into the above equation, we obtain the width as 22.3 nm for (00,2) lattice planes of carbon nanotubes. Looking at figure 3, the area of disappearance is only one. This means that the nanotube is not so tilted from normal to the electron incidence and the height difference of the tube between the left-hand side and the right-hand side margins of this photographic view is less than 20 nm. These data are considered to be a kind of direct measurement of depth in TEM observations in the case of small C_s-values.

Some discussions have already been made about the origins of lattice fringe contrast obtained by C_s-corrected HRTEM. It was reported that lattice fringes were actually observed near just-focus even with $C_s = 0$ for silicon and other crystals. The phenomenon was interpreted in terms of an amplitude contrast [16, 17]. In order to clarify the problem, we need to study the lattice images of very thin crystals treated as pure-phase objects or weak-phase objects without the amplitude contrast term. Thin amorphous carbon films are insufficient for this purpose because the amplitude term of the films is not easy to define and granular images due to the amorphous structures always appear. In the present study we have observed carbon nanotubes by using a C_s-corrected TEM as explained below.

Figure 4 shows schematic cross-sectional views of a perfect crystal such as silicon (a) and the present carbon nanotube (b). The carbon nanotube is composed of cylindrically bent graphite crystals (graphene layers). The Bragg condition of the (00,2) reflection giving lattice fringes of 0.335 nm spacing is satisfied only for a small part of the cylindrical tube, as indicated by the thick black arrow in figure 4(b), in contrast to the perfect silicon crystal in figure 4(a). This small part is related to the small distance along
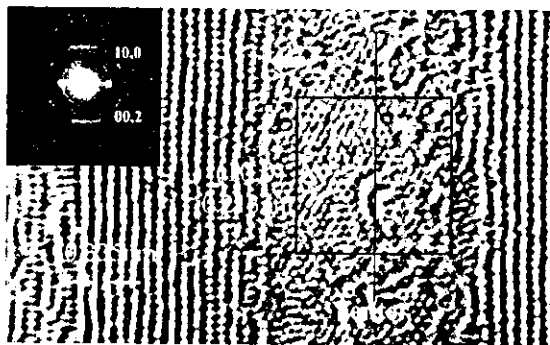
Figure 5. High-resolution electron micrograph of a multi-wall carbon nanotube (MWCNT), showing a network structure of (10,0) lattice planes from the side walls of the tube.

the z-direction, which decreases the dynamical diffraction effect and the creation of amplitude contrast. Kambe discussed the amplitude modulation below [011] oriented germanium single crystals in terms of 'the image of individual Bloch waves' created by dynamical diffraction [18]. A carbon nanotube is not such a case, as explained in figure 4. The tube is considered to be an ideal sample which can be treated as a weak-phase object, also because it is composed of a light element having a small atomic scattering factor. Despite the carbon nanotubes having no amplitude contrast modulation, we can clearly observe (00,2) lattice fringes in the present experiment. This is a phase contrast obtained by slight defocusing. It is noted in C_s-corrected TEM with a very small C_s value that the Scherzer defocus $(=1.18\sqrt{C_s\lambda})$ which is a condition of phase contrast imaging, occurs near the just-focus. Considering this fact, it is probable that most of lattice fringes of crystalline samples observed previously by C_s-corrected TEM are those obtained by phase contrast, although those crystalline samples have an amplitude modulation as shown in Kambe's paper for axial electron incidence. Since the focus difference as $d^2/2\lambda$ amounts to 19.5 nm for the (111) lattice planes of silicon, it is not easy to discriminate between 'in-focus' or 'slightly out of focus' in actual experimental conditions.

3.2. Improvement of image resolution in lateral directions

Figure 5 shows a high-resolution TEM image and the selected area diffraction pattern of an MWCNT of 6.2 nm inner diameter and 16.1 nm outer diameter, taken with the 200 kV C_s-corrected TEM. The image contrast in the centre area of the side wall shows (10,0) lattice fringes from the curved graphene (00,1) layers (marked as $d_{10,0}$ = 0.213 nm). Figure 6(a) shows an enlarged image of a black-squared area in figure 5 after Fourier filtering. The filtering was performed by using circular apertures containing diffraction spots such as 10,0, as shown in the inset. Hexagonal arrangements of black dots are clearly seen in some areas as indicated by the white arrows. Since the area is located at the centre of the side wall of the nanotube, the electrons are almost incident normal to the (00,1) graphene layers. The variation of appearance of the black dots observed here may be due to (1) a local stacking disorder as shown later in figure 7 or (2) a moiré fringe effect from the superposition of the lower and upper layers of the rolled-up
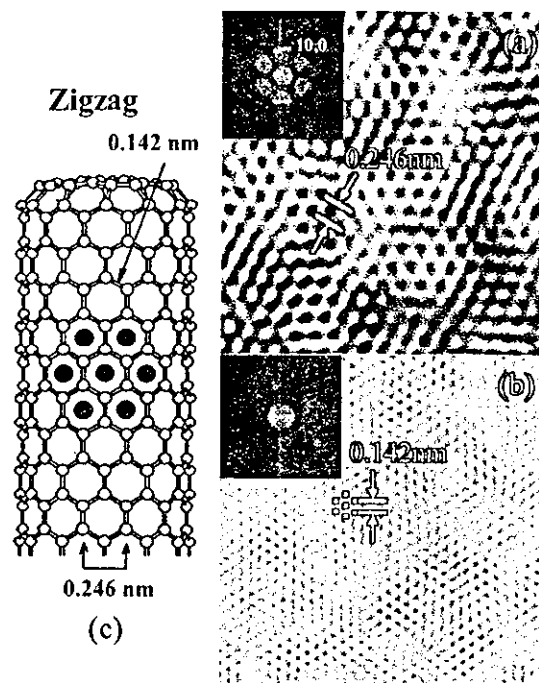

Figure 6. Enlargement of a black-squared area in figure 5 after Fourier filtering, showing (10,0) lattice fringes more clearly from the graphene layers (a), another filtered image using 11,0 spots, showing the finer structural information down to 0.14 nm (b), and an illustration of the structure of a zigzag type carbon nanotube (c).

carbon nanotube. Cullen *et al* obtained a similar image contrast previously and discussed the origin as the moiré effect [19]. In the present case, however, the variation is irregularly spaced, which suggests that the origin is due to disorder. Some of the disorder may come from irradiation damage by the incident electrons. The wavy contrast observed in the right-hand side area in figure 5 may be coming from amorphous materials attached to the nanotube.

The separation of dots in figure 6(a) is 0.246 nm, which corresponds to $\sqrt{4/3}$ times the spacing of the (10,0) planes, 0.213 nm. Comparing the arrangement of black dots and the illustration of the atomic arrangement of a 'zigzag-type' carbon nanotube in figure 6(c) [20], we conclude that the tube has the same atomic structure as the illustration. It is noted here that the conclusion could be drawn if the graphene layers are slightly tilted to the electron incidence, because the information can be deduced even from 'lattice fringe images'.

Figure 6(b) shows another Fourier-filtered image using 11,0 spots of the exact same area as in figure 6(a), which gives a contrast of dots separated by 0.142 nm with local variations. For the processing, we have made efforts to minimize the effects of the filtering by smaller apertures. The spacing corresponds to the bond length of hexagons of carbon atoms, but is not interpretable as the image contrast of the hexagons themselves because the contrast is a kind of lattice fringe.

Figure 7 is another image showing a stacking disorder inside the side wall in a cross-sectional view. This kind of information on stacking disorder in nanotubes is clearly visualized for the first time in the present observation.

It should be emphasized that the image in figure 5 was taken near the Scherzer defocus, slightly underfocused from
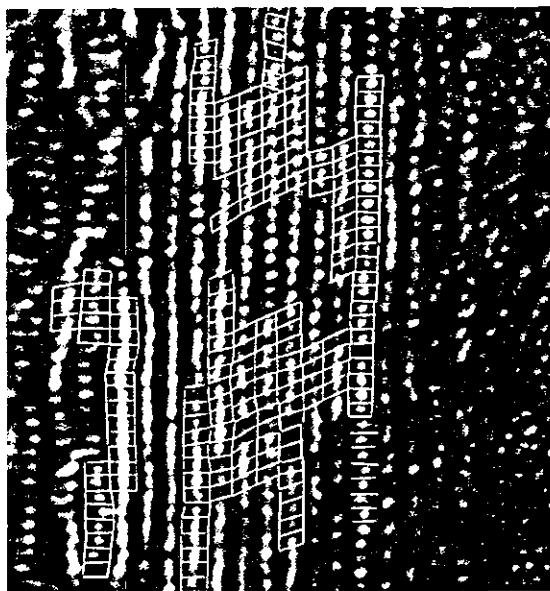
Figure 7. Enlargement of the left-hand side of figure 5 adding the squares of a unit cell, showing a stacking disorder in a cross-sectional view.

the Gaussian focus. The Fresnel fringes appearing at the boundaries of the inner wall are minimized, as indicated by the white arrow in figure 5. The images in figures 5–7 suggest the possibility of resolving the arrangement of carbon atoms in tubular materials by using a C_s-corrected TEM, although the imaging conditions should be carefully tuned [19]. Figure 8 is a 200 kV image simulation of an (00,1) graphite crystal as a model of curved graphene layers with normal electron incidence by using typical lens parameters such as $C_s = 10 \mu m$ and energy spread $\Delta = 2$ nm; the resolution of the hexagon of carbon atoms is indicated by black arrows in figure 8(a). The image contrast in figure 8(a) with 6.13 nm underfocus is comparable to figures 6(a) and (b).

Based on the present observation of MWCNTs by the C_s-corrected TEM, we could have a near-future insight about the electron microscopy of carbon nanotubes. The imaging characteristics of thin MWCNTs can be described successfully in terms of the Fourier image, as shown in figure 2, because they are treated as a weak-phase object without strong dynamical diffraction effect. The problem considered here is which branch we should use for the imaging of the MWCNTs: the

amplitude contrast branch or phase contrast one? Indeed, specially designed phase plates inserted in the back-focal plane of the objective lens are necessary for the use of the amplitude contrast branch, similarly to the Zernike phase optical microscope. Danev et al fabricated a phase plate for TEM by using a thin carbon film with a small hole drilled by FIB [21]. It is not still clear if the phase plate is applicable to observation down to 0.1 nm resolution or not.

Our tentative way is therefore to use the phase contrast branch $n = 0$ in figure 2, which almost approaches the y-axis in the diagram in the case of small C_s. The phase contrast transfer function $\sin \chi$ is, however, depressed at a low scattering angle region (large d in figure 2). A correction by using a Wiener filter such as $1/(\sin \chi + \text{small c.c.})$ is helpful, where χ is the wave aberration function of objective lens [22]. The filter was proved to be usable in the case of weakly scattering objects, not weak-phase objects [15].

It is also noted that a decrease of the accelerating voltage from 200 kV to 120 or 100 kV is necessary from the viewpoint of the image contrast of carbon atoms and decrease of irradiation damage. For the image contrast, Reimer calculated that decreasing the voltage is effective for increasing the phase contrast using elastic scattering from atom clusters and crystallites, not single atoms [10]. Figure 9 shows another simulation of C_s-corrected TEM images of a graphite crystal at an accelerating voltage of 120 kV with $C_s = 10 \mu m$ and defocus spread, $\Delta = 3$ nm. In this accelerating voltage also, the hexagonal arrangement of carbon atoms separated by 0.142 nm is discriminated. The instrumental condition is realized without so much difficulty from the viewpoint of recent technology. The energy spread, $\Delta = 3$ nm, corresponds to an energy fluctuation of 0.35 eV, assuming that the chromatic aberration constant $C_c = 1$ mm. This value can be realized by a cold field emission gun without a monochromator.

4. Concluding remarks

In the present study a spherical aberration corrected TEM was applied for the first time to multi-wall carbon nanotubes in order to improve the depth and lateral resolutions of observation and to reconsider the origin of lattice fringes observed by the C_s-corrected TEM. The improvement of the depth resolution has given one a possibility to measure the local height of the nanotubes like an altimeter of an aircraft, and that in lateral resolution has enabled one to determine directly the chirality and see the finer structures of the tubes at
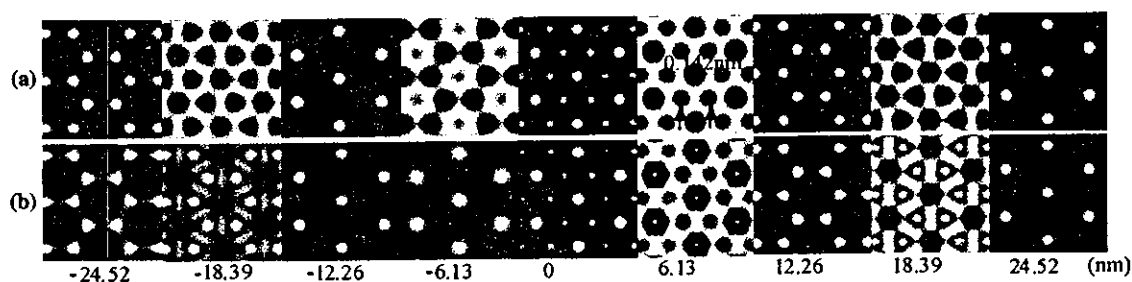

Figure 8. Image simulation of a (00,1) graphite crystal of 3.4 nm (5 × c) (a) and 6.8 nm (10 × c) (b) thickness under conditions of $E = 200$ kV, $C_s = 10 \mu m$, energy spread $\Delta = 2$ nm and defocus conditions (nm, positive = underfocus) written in figures. These images show the possibility of resolving six-member rings of carbon atoms as indicated by the black arrows.
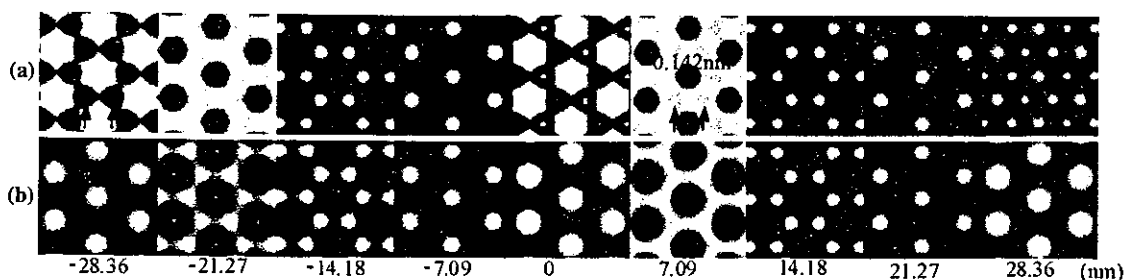
Figure 9. Image simulation similar to figure 8 at 120 kV accelerating voltage.

a resolution better than 0.14 nm. The high resolution imaging characteristics for carbon nanotubes using C_s-corrected TEM was discussed in a comparison between 200 and 120 kV accelerating voltages. The C_s-corrected HRTEM opens a new stage of structural study of nano-tubular materials.

Acknowledgments

References

[1] Pennycook S J and Jesson D E 1990 *Phys. Rev. Lett.* **60** 938

[2] Haider M, Rose H, Uhlemann S, Kabius B and Urban K 1998 *J. Electron Microsc.* **47** 395

[3] Tanaka N, Yamasaki J, Usuda K and Ikarashi N 2003 *J. Electron Microsc.* **52** 69

[4] Tanaka N, Yamasaki J, Fuchi K and Tekeda Y 2004 *Microsc. Microanal.* **10** 139

[5] Jia C L, Lentzen M and Urban K 2003 *Science* **299** 870

[6] Odom T M, Huang J L, Kim P and Lieber C M 1998 *Nature* **391** 62

[7] Tanaka N, Hirayama T, Ikuhara Y, Hosokawa F and Naruse M 2002 *Proc. 15th ICEM (1–6 September 2002, Durban, South Africa)* vol 3 (Onderstepoort, South Africa: Microscopy Society of Southern Africa) p 37

[8] Hosokawa F, Tomita T, Naruse M, Honda T, Hartel P and Haider M 2003 *J. Electron Microsc.* **52** 3

[9] Zemlin F, Weiss K, Schiske P, Kunath W and Hermann K H 1977 *Ultramicroscopy* **3** 49

[10] Reimer L 1984 *Transmission Electron Microscopy* (Berlin: Springer)

[11] Ishizuka K 1982 *Acta Crystallogr.* A **38** 773

[12] Iijima S 1990 *Nature* **354** 56

[13] Cowley J and Moodie A F 1957 *Proc. Phys. Soc.* **70** 486

[14] Thon F 1966 Z. *Naturf.* a **21** 179

[15] Tanaka N and Hu J J 1998 *J. Electron Microsc.* **47** 217

[16] Lenzen M, Jahnen B, Jia C L, Thust A, Tillmann K and Urban K 2002 *Ultramicroscopy* **92** 2333

[17] Hutchison J L, Titchmarsh J M, Cockayne D J H, Mobus G, Hetherington C J, Doole R C, Hosokawa F, Hartel P and Haider M 2002 *Proc. Microsc. Microanal. (Quebec, Canada)* vol 8 (Cambridge: Cambridge University Press) p 10

[18] Kambe K 1982 *Ultramicroscopy* **10** 223

[19] Cullen S L, Boothroyd C B and Humphreys C J 1994 *Ultramicroscopy* **56** 127

[20] Dresselhaus M S, Dresselhaus G and Avouris Ph (ed) 2001 *Carbon Nanotubes* (Berlin: Springer)

[21] Danev K and Nagayama K 2001 *Ultramicroscopy* **88** 243

[22] Tanaka N, Maki T, Mihama K and Tsuno K 1989 *J. Electron Microsc.* **38** 54

Large-Scale Production of Ba^{2+}–Alginate-Coated Vesicles of Carbon Nanofibers for DNA-Interactive Pollutant Elimination

Bunshi Fugetsu,* Shuya Satoh, Toshikazu Shiba,[1,2,3] Taeko Mizutani,[2] Yoshinobu Nodasaka,[4]
Keiji Yamazaki,[5] Kiyoko Shimizu,[6] Masanobu Shindoh,[4] Ken-ichiro Shibata,[4] Norio Nishi,
Yoshinori Sato,[7] Kazuyuki Tohji,[7] and Fumio Watari[4]

Graduate School of Environmental Earth Science, Hokkaido University, Sapporo 060-0810

[1]Regenetiss Co., Ltd., 1-5-17, Okaya, Akabane, Nagano 394-0002

[2]Millennium project, Frontier Research Division, Fujirebio Inc., 51, Komiya, Hachioji, Tokyo 192-0031

[3]Department of Oral and Maxillofacial Surgery, Matsumoto Dental University School of Dentistry, Shiojiri 399-0781

[4]Graduate School of Dental Medicine, Hokkaido University, Sapporo 060-8586

[5]Otsuka Electronic Co., Ltd., 1-6 Azuma-cho, Hachioji, Tokyo 192-0082

[6]Hokudo Co., Ltd., Bioscience Division, Abuta-cho, Abuta-gun, Hokkaido 049-5613

[7]Graduate School of Environmental Studies, Tohoku University, Sendai 980-8579

Received March 24, 2004; E-mail: hu@ees.hokudai.ac.jp

Ba^{2+}–alginate coated vesicles (Ba^{2+}–ALG) containing highly dispersed carbon nanofibers (CNFs) were successfully produced for the first time using an encapsulation technique. These Ba^{2+}–ALG/CNFs composite vesicles showed high capabilities in trapping DNA-interactive types of chemicals. For example, 10.0 mL of the vesicles took 0.43 μmol of ethidium ions up from contaminated water within 8 min. Biocompatibility experiments performed in vitro and in vivo provided promising results, suggesting potential applications in in-situ environmental remediation. Kilogram quantities of the Ba^{2+}–ALG/CNFs composite vesicles can be produced within a few hours.

DNA-interactive chemicals, such as ethidium ions, are capable of interacting with DNA with high affinities. This type of chemical is responsible for causing DNA damage and/or frame-shift mutagenesis induction, also known as the key-initial processes in carcinogenesis.[1–3] We demonstrated in our previous studies[4–7] that materials having DNA as functional sites, such as Ba^{2+}–alginate coated vesicles containing double-stranded DNA (purified from salmon milt), are capable of trapping this type of chemical from contaminated waters. DNA leakage, which results in performance degradation and a limited lifetime of the functional materials, however, has been a major drawback of these materials.[8]

In this study, we use carbon nanofibers (CNFs) as the functional sites for trapping DNA-interactive chemicals. Adsorbents with high capabilities were obtained successfully by encapsulating the highly dispersed CNFs in Ba^{2+}–alginate coated vesicles. In recent years, carbon nanomaterials, especially the so-called carbon nanotubes (CNTs), discovered first by Iijima,[9,10] have attracted great attention due to their unusual morphologies. An analytical chemical study carried out by Cai and co-workers[11] demonstrated that multi-walled CNTs (MWCNTs) can trap some aromatic chemicals, such as bisphenol A, 4-*n*-nonylphone, and 4-*tert*-octylphenol from contaminated water by passing the contaminated water through a cartridge filled with MWCNTs. The targeted species trapping was achieved by the hexagonally arrayed carbon atoms of the

graphite sheets of the external faces of the MWCNTs.[11,12]

CNFs are built up also by hexagonally arrayed carbon atoms with the 002 planes being piled up along the direction of the fiber axis. These graphite platelets stacked in a perfectly arranged conformation resulted in generating a unique system comprising entirely of slit-shaped wall-nanopores.[13] If these wall-nanopores can be also activized for trapping DNA-interactive chemicals, higher elimination efficiencies than can be achieved with MWCNTs can be obtained.

Experimental

Dispersing CNFs Using Alginate. Sodium alginate (viscosity and pH at 20 °C were 300–400 cP and 6.0–8.0, respectively, for a 20.0-mg/mL aqueous solution), the dispersing agent used throughout this study, was obtained from Wako Chemical Industries (Osaka, Japan). Sodium alginate (Na$^+$–ALG) was dissolved in deionized water to prepare the aqueous Na$^+$–ALG solutions. CNFs (diameter, 50–250 nm; length, 2–15 μm; purity > 90%; those produced in the laboratory were based on the chemical vapour deposition;[14] Figs. 1A and B show the SEM and TEM images) were added to the aqueous Na$^+$–ALG solutions and were well-mixed by a combination of high-shear mixing and sufficient ultra-sonication. The aqueous Na$^+$–ALG/CNFs colloidal solutions were centrifuged at 4000 rpm for 30 min. A very small amount of black precipitate from the aqueous solution was observed (which was removed from the aqueous colloidal solution).
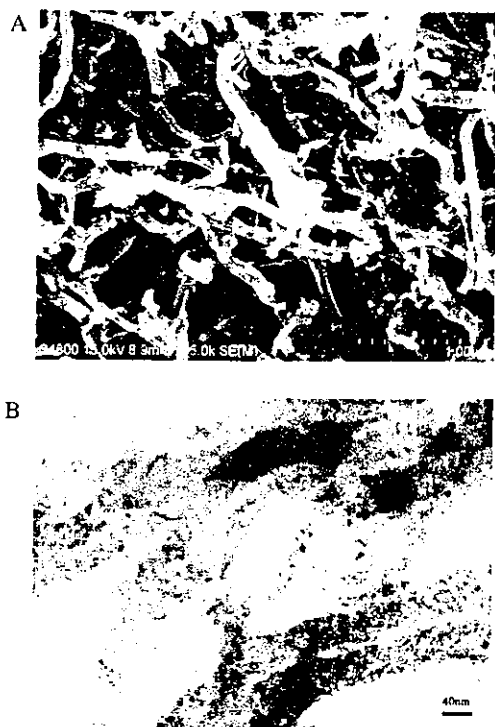
Fig. 1.   SEM image (Fig. 1A) and TEM image (Fig. 1B) of the synthesized/purified carbon nanofibers (CNFs). SEM (Hitachi S4800) was operated at 15 kV; while TEM (Hitachi H-800) was operated at 200 kV. Platelet CNFs in which the 002 planes are piled up along the fiber axis direction together with the herringbone CNFs in which the 002 planes are distrusted on the two sides at an angle with respect towards the fiber axis were observed.
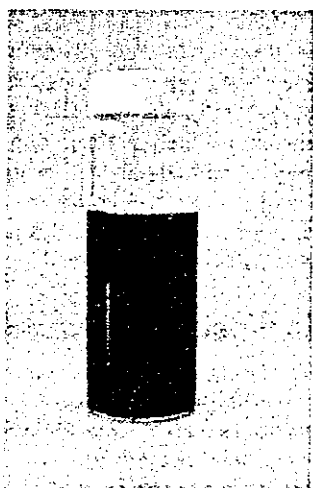

Fig. 2.   A photograph of a 100-mL glass-vial containing CNFs being highly dispersed in the Na$^+$–ALG aqueous solution. Concentrations of CNFs and Na$^+$–ALG were 0.5 mg/mL and 20.0 mg/mL, respectively.

Figure 2 shows a photograph of a 100-mL glass vial containing the aqueous Na$^+$–ALG/CNFs colloids. Concentrations for CNFs and Na$^+$–ALG were 0.50 mg/mL and 20.0 mg/mL, respectively. No precipitation was observed from this aqueous colloidal solution during a three-week observation period. Aqueous Na$^+$–ALG/

CNFs colloids with a high uniformity were obtainable up to a concentration of 1.0 mg/mL for CNFs using the 20.0 mg/mL aqueous Na$^+$–ALG solution as the dispersing solution. The uniformity of the aqueous Na$^+$–ALG/CNFs colloids was measured by calculating the linearity of the calibration curve for CNFs in the Na$^+$–ALG/CNFs colloidal solutions using UV–vis at 260 nm as the detection. Zeta potentials of the aqueous Na$^+$–ALG/CNFs colloids were measured using an electrophoretic light scattering spectrophotometer (ELS-8000, Otsuka Electronics, Osaka, Japan). FT-IR spectra of Na$^+$–ALG in the aqueous Na$^+$–ALG/CNFs colloids were measured using a FT/IR-460 (Jasco, Tokyo, Japan).

Biocompatibility Tests. Normal human fibroblasts (HF) were used as the typical cells (obtained from BioWhitteker Inc.) to perform the in vitro experiments. A MTS [3-(4,5-dimethylthiazol-2-yl)-5-(3-carboxymethoxyphenyl)-2-(4-sulfophenyl)-2H-teraazolium] cell proliferation assay kit was purchased from Promega. Dulbecco's modified Eagle's minimal essential medium (D-MEM), L-glutamine, and fetal bovine serum (FBS) were purchased from Sigma. The aqueous Na$^+$–ALG/CNFs colloidal solution containing 1.0 mg/mL of CNFs and 20.0 mg/mL of Na$^+$–ALG was diluted to 1/10, 1/100, and 1/1000 with D-MEM containing 5.0% FBS and 50 μg/mL kanamycin. An aqueous solution containing Na$^+$–ALG alone (20.0 mg/mL; the control vehicle) was also diluted to the same degree with the same medium as for Na$^+$–ALG/CNFs. HF were seeded in 96-multiwell plates at 2 × 10^3 cell/well and maintained in 200 μL D-MEM containing 10% FBS and 50 μg/mL kanamycin for 3 days at 37 °C. The medium was replaced with the medium containing the Na$^+$–ALG/CNFs or the control vehicle and were further incubated for 1–7 days at 37 °C. After the incubation, cell growths were evaluated by MTS assay. For the MTS assay, the medium was substituted for 100 μL of Eagle's minimal essential medium (without Phenol Red) containing 333 μg/mL MTS and 25 μM phenazine methosulfate solution. After incubation for 2 h at 37 °C, the absorbance at 485 nm of each well was measured. The cell growth was calculated from the value of A_{485} at 2 h after MTS processing.

Eight 8-week-old Jcl:SD male rats (purchased from Clea Japan, Inc.) were used to perform the in vivo experiments. These rats were quarantined and acclimatized for six days. One was used without any administration while the others were single dosed orally using a stomach tube. The dose values were 10 mg/kg for CNFs and 200 mg/kg for Na$^+$–ALG of the body weight. Gross observations and body weights were recorded weekly. During the term of observation, animals were starved for 16 h, anesthetized, and then blood and serum samples were collected. Necropsy was also performed for observing changes in the glandular stomach.

Encapsulating CNFs. An IER-20® system (Inotech, Dottikon, Switzerland) was used for encapsulating CNFs to form Ba^{2+}–alginate coated vesicles. The IER-20® system consisted of a syringe and a pump, a pulsation chamber, a vibration system, a nozzle, an electrode, an ultra-sonication vibration system along with an electrostatic supply system, and an O-ring-shaped electrode. The aqueous Na$^+$–ALG/CNFs colloids were forced into the pulsation chamber using the syringe pump. These aqueous colloids were then passed through the precisely drilled sapphire-nozzle (nozzle size, 300 μm) and were separated into droplets of equal size on exiting the nozzle. These droplets passed through the electrostatic field between the nozzle and the ring electrode and acquired electrostatic charges on their surfaces. Electrostatic repulsion forces dispersed the droplets as they fell in to the hardening solution, i.e., the aqueous solution containing 100 mM of barium chloride. The resultant vesicles were rinsed thoroughly

with deionized water using a 100 μm mesh sieve. Reference vesicles (without containing CNFs) were also prepared under these identical experimental conditions.

Adsorptive Capability Studies.   Three 45-mL conical-bottomed tubes, each containing 10.0 mL of the reference vesicles, the vesicles containing highly dispersed CNFs, and the vesicles containing low-dispersed CNFs, were held vertically using a tube-stand, 15.0 mL of a 30.0 μM ethidium bromide aqueous solution were then added to each of the tubes. At about ten minutes after mixing the ethidium solution with the vesicles, approximately 3 mL of the bulk-phase solutions were collected and measured using a UV–vis spectrometer (Jasco UV-550).

Results and Discussion

Insights in to the Dispersion Mechanism.   A characteristic absorption band derived from the CNFs is seen at around 260 nm for the aqueous Na^+–ALG/CNFs colloidal solutions. The linearity, r^2, of the calibration curve for CNFs in the aqueous Na^+–ALG/CNFs colloidal solutions at 260 nm was found to be better than 0.9986, indicating a high uniformity of the aqueous Na^+–ALG/CNFs colloidal solutions. Samples used for deriving the calibration curve were the aqueous Na^+–ALG solutions containing 0, 0.1, 0.2, 0.3, 0.4, and 0.5 mg/mL of the CNFs with the concentration of Na^+–ALG in each sample being fixed at 20.0 mg/mL. The stability of the aqueous Na^+–ALG/CNFs colloids was measured by calculating the concentration of the CNFs versus the sediment time, similar to the method reported by Jiang and co-workers.[15] Changes in the CNF concentrations were found to be smaller than 0.4% over three-weeks at room temperature.

The zeta potentials of the Na^+–ALG/CNFs colloids were measured. Zeta potential values, ζ, were calculated from the particle velocities based on the Helmholtz–Smoluchowski equation ($\zeta = 4\pi\mu\eta/D$, where, μ, η, and D are the electrophoretic mobility, viscosity, and the dielectric constant of the liquid in the boundary layer, respectively).[16] As can be seen from the ζ vs pH plots (Fig. 3), the maximum ζ value of the Na^+–ALG/CNFs colloids was −58.03 mV. This again indicates a high stability (repulsion) of the Na^+–ALG/CNFs col-
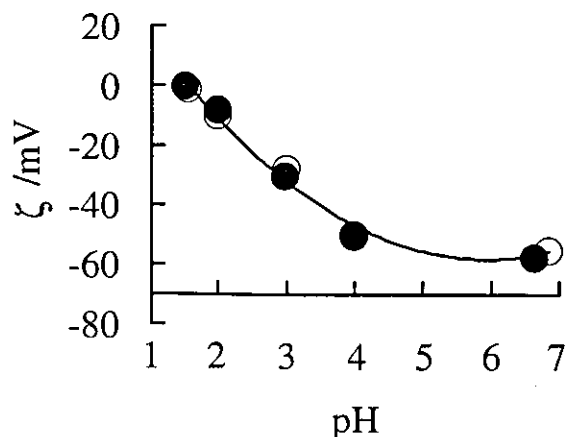
loids. The ζ vs pH plots (Fig. 3) for the Na^+–ALG/CNFs colloids and that for the aqueous solution containing Na^+–ALG alone were virtually identical, indicating the zeta potentials of the Na^+–ALG/CNFs colloids are governed by alginate ions. A decrease in the absolute value of ζ is seen for both samples as the pH decreased (pH of the samples were adjusted using 1.0 mol L^{-1} HCl) for all pH value studies. This implies that alginate attached tightly to the CNFs throughout the entire pH range. Note the Na^+–ALG/CNFs colloids condensed as the pH reached smaller values (2.99 and 1.51).

Alginate is a linear, water-soluble 1,4-linked copolymer of β-D-mannuronate (M) and/or α-L-guluronate (G). M and G can be arranged in homopolymeric [poly(β-D-mannosyluronate, M-M-M)] and poly(α-L-gulosyluronate, G-G-G) or heteropolymeric (M-G-M) blocks,[17,18] as illustrated in Fig. 4. FT-IR spectra of alginate alone (the reference sample) and the Na^+–ALG/CNFs colloids were measured, as shown in Fig. 5. The typical characteristic bands found for the reference
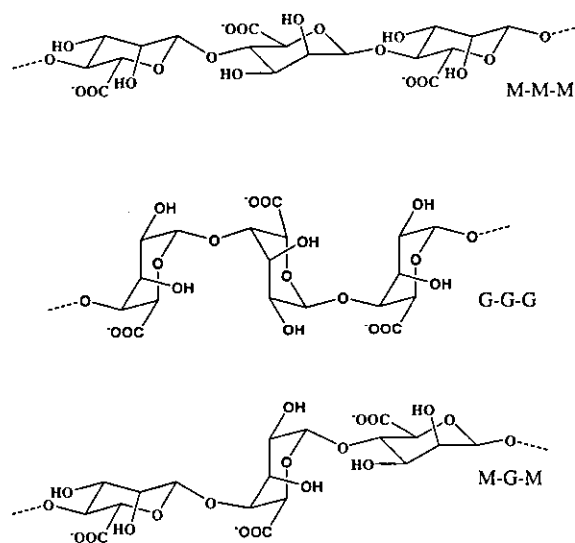

Fig. 4.   Three possible molecular structures of alginate. The homopolymeric M-M-M- and G-G-G- and M-G-M-linked alginate.
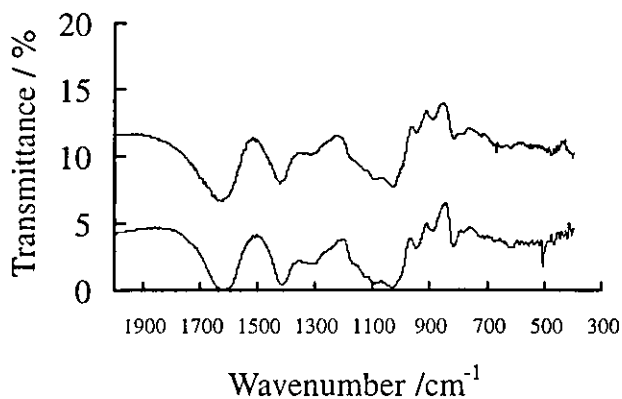

Wavenumber /cm^{-1}

Fig. 5.   FT-IR spectra of Na^+–ALG (upper-trace) and that of Na^+–ALG/CNFs colloids (lower-trace) in the solid state using the potassium bromide (KBr) pellet method.

pH

Fig. 3.   Zeta potential (ζ) of the aqueous Na^+–ALG/CNFs colloids (●, 0.50 mg/mL for CNFs and 20.0 mg/mL for Na^+–ALG) and ζ of the aqueous solution containing Na^+–ALG alone (○, 20.0 mg/mL of Na^+–ALG) versus pH.